

## Experimental and theoretical comparison of different optical excitation schemes for a compact coherent population trapping Rb vapor clock

This content has been downloaded from IOPscience. Please scroll down to see the full text.

2017 Metrologia 54 418

(<http://iopscience.iop.org/0026-1394/54/4/418>)

View [the table of contents for this issue](#), or go to the [journal homepage](#) for more

Download details:

IP Address: 129.105.5.12

This content was downloaded on 14/06/2017 at 20:22

Please note that [terms and conditions apply](#).

# Experimental and theoretical comparison of different optical excitation schemes for a compact coherent population trapping Rb vapor clock

Z Warren<sup>1</sup>, M S Shahriar<sup>2,3</sup>, R Tripathi<sup>1</sup> and G S Pati<sup>1</sup>

<sup>1</sup> Department of Physics and Engineering, Delaware State University, Dover, DE 19901, United States of America

<sup>2</sup> Department of Electrical Engineering and Computer Science, Northwestern University, Evanston, IL 60308, United States of America

<sup>3</sup> Department of Physics and Astronomy, Northwestern University, Evanston, IL 60308, United States of America

E-mail: [zack.a.warren@gmail.com](mailto:zack.a.warren@gmail.com)

Received 17 January 2017, revised 25 April 2017

Accepted for publication 12 May 2017

Published 14 June 2017



## Abstract

We have investigated, theoretically as well as experimentally, the relative merits and demerits of using three different optical configurations for a compact coherent population trapping (CPT) vapor clock using <sup>87</sup>Rb. These correspond to the following choices of polarizations for the two Raman beams: lin || lin, ( $\sigma$ ,  $\sigma$ ), and push–pull optical pumping (PPOP), applied on the D1 manifold. We have used a multi-level atomic model to study the dependence of the CPT spectrum on axial as well as transverse magnetic fields for these three schemes. Corresponding experimental studies have been performed using a laboratory scale CPT clock employing a two cm long, isotopically pure rubidium cell, loaded with a buffer gas. We observed a CPT contrast close to 20% with a sub-kilohertz linewidth by adopting the PPOP scheme. We discuss the strengths and weaknesses of each of the three optical excitation schemes, and present frequency-stability measurement data for the prototype clock.

Keywords: atomic clocks, atomic coherence, atomic and molecular physics, optical spectroscopy, frequency standards

(Some figures may appear in colour only in the online journal)

## 1. Introduction

Compact atomic clocks are being developed for high performance timekeeping applications in ground- and space-based communications and navigation systems [1–6]. Vapor cell atomic clocks designed using coherent population trapping (CPT) are suitable for such applications, and have been studied in miniaturized forms for a number of years [7–14]. Additionally, cold atom systems are being studied for compact atomic clock development [15, 16]. The optical excitation scheme commonly used in the CPT clock employs circularly ( $\sigma^+$  or  $\sigma^-$ ) polarized laser light for interrogating rubidium

atoms. This light is produced by a frequency-modulated laser beam. It is known that circularly polarized light pumps a significant fraction of the atoms into Zeeman edge (or trap) states, reducing contrast in the CPT signal. This can be prevented by using, on each leg of the  $\Lambda$  system, linearly polarized fields having both  $\sigma^+$  and  $\sigma^-$  circular components. However, a pure dark state cannot be formed in the  $m_F = 0$  ground state sub-levels of alkali D1 manifold by a pair of parallel, linearly polarized (lin || lin) CPT fields. This is because the dark states corresponding to the circular fields,  $|\text{dark}_{\sigma^+}\rangle$  and  $|\text{dark}_{\sigma^-}\rangle$  are non-identical, due to opposite signs of matrix element ratios associated with  $\sigma^+$  and  $\sigma^-$  transitions [17–20]. However, this

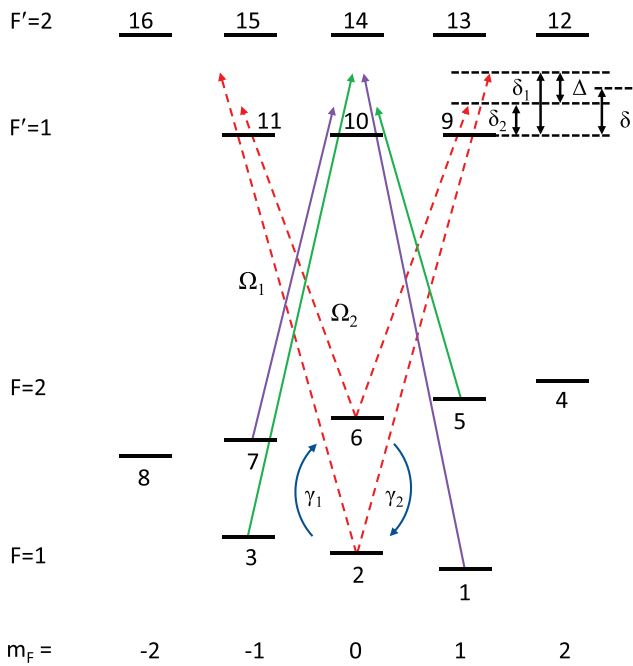


**Figure 1.** Raman excitation in a multi-level atomic system consisting of all the energy levels in the D1 manifold of  $^{87}\text{Rb}$  atoms. The hyperfine splitting between  $|F = 1\rangle$  and  $|F = 2\rangle$  ground states is 6.8347 GHz, and between  $|F' = 1\rangle$  and  $|F' = 2\rangle$  excited states is 814.5 MHz. For the purpose of theoretical modeling, the magnetic sublevels in the F-states are designated by a sequence of numbers from one to sixteen.

problem can be circumvented by making use of a pair of orthogonal, linearly polarized (lin  $\perp$  lin) CPT fields, enabling the formation of a pure dark state in the  $m_F = 0$  ground state sublevels [21]. A practical constraint in using this approach is due to the fact that one cannot generate lin  $\perp$  lin polarization states by frequency-modulating a laser directly. Alternative methods, such as push-pull optical pumping (PPOP) and counter-propagating circularly polarized beams have been investigated for generating CPT resonance with high contrast [22–26]. The polarization states of the optical fields employed for PPOP scheme are equivalent to those corresponding to the use of the lin  $\perp$  lin scheme [24]. Other methods, such as four-wave-mixing and differential magneto-optical rotation (MOR) have also been proposed for producing background-free CPT resonance with high contrast [27–33].

The need for miniaturization of the vapor cell atomic clock restricts the size and complexity of its operating components. Keeping this in mind, we have considered three primary polarization schemes, ( $\sigma$ ,  $\sigma$ ), lin  $\parallel$  lin, and PPOP (which is the same as lin  $\perp$  lin) for our investigations in order to establish which is best suited for meeting the restrictions encountered in compact CPT clock development. We have studied experimentally the performance of these three schemes for generating high contrast, magnetically insensitive CPT resonances in D1 atomic transitions of  $^{87}\text{Rb}$  atoms. We have also developed a multi-level atomic model for theoretically investigating these polarization schemes by including all the Zeeman sublevels in  $^{87}\text{Rb}$  D1 transitions. The results obtained from our model

show relative strengths of CPT resonances formed by these polarization schemes. The model also allows us to examine the CPT spectrum in the presence of a transverse magnetic field. To study experimentally the performance of these polarization schemes, a small (2 cm in length) rubidium cell is used to develop a CPT clock prototype. Our study shows that the polarization schemes have varying benefits and drawbacks with regard to increased clock stability, noise reduction, and compactness. Correlated laser noise and electronic noise can be eliminated in the MOR-CPT scheme by subtracting the detector outputs [28]. We observed that the lin  $\parallel$  lin polarization scheme combined with differential MOR can produce dispersive CPT signal with high signal-to-noise ratio, but can reduce the mid- or long-term frequency stability of the clock, as it exhibits high sensitivity to the magnetic field.

The rest of the paper is organized as follows. In section 2, we first discuss the multi-level atomic model developed for studying CPT resonance using different polarization schemes. In section 3, we describe the experiments conducted with a small rubidium cell. In section 4, we present experimental results, comparing the performances of the three polarization schemes in a CPT rubidium clock.

## 2. Multi-level atomic model

We created a comprehensive atomic model using the Liouville density-matrix equation [34, 35], taking into account all relevant Zeeman sublevels. This model is used to study CPT resonances formed by the two-photon Raman excitation with two laser fields at frequencies  $\omega_1$  and  $\omega_2$  in the D1 manifold of  $^{87}\text{Rb}$  atoms.

Figure 1 shows all sixteen Zeeman sublevels in our model, with the hyperfine ground states  $|F = 1, 2\rangle$  coupled to the hyperfine excited states  $|F' = 1, 2\rangle$  by the applied fields. Each hyperfine state consists of magnetic  $m_F$  sublevels which are designated by the number sequence from 1 to 16. The evolution of the atomic system is governed by the Liouville equation:  $\frac{\partial \rho}{\partial t} = -\frac{i}{\hbar} [H\rho - \rho H^\dagger] + L$ , where  $\rho$  is the density operator,  $H$  is the semi-classical, non-Hermitian Hamiltonian, and  $L$  represents the source matrix, as defined in detail next. The non-Hermitian Hamiltonian,  $H = H_A + H_B + H_\Gamma$ , is expressed as the sum of three parts:  $H_A$  represents the internal atomic energy plus the energy due to interaction with the laser fields,  $H_B$  represents the energy due to interaction with the magnetic field, and  $H_\Gamma$  (which is complex) accounts for the decays of atomic states. Under the rotating wave approximation, and in the rotating wave picture,  $H_A$  (with  $\hbar = 1$ ) for the sixteen-level system can be described as:

$$H_A = \frac{\Delta}{2} \sum_{m=1}^3 s_{m,m} - \frac{\Delta}{2} \sum_{m=4}^8 s_{m,m} - \delta \sum_{m=9}^{16} s_{m,m} + \left( \frac{\Omega_1}{2} \sum_{m=1}^3 \sum_{n=9}^{16} d_{mn} s_{m,n} + \frac{\Omega_2}{2} \sum_{m=4}^8 \sum_{n=9}^{16} d_{mn} s_{m,n} + h.c. \right) \quad (1)$$

where  $s_{m,n} = |m\rangle\langle n|$  is defined as the outer product matrix with  $|m\rangle$  as the  $m$ th energy state represented by a  $(16 \times 1)$  column vector,  $\Delta = \delta_1 - \delta_2$  is the difference frequency detuning between the CPT fields, with  $\delta_1$  and  $\delta_2$  (shown in figure 1) corresponding to respective single photon detuning for the laser frequencies  $\omega_1$  and  $\omega_2$ ,  $\delta = (\delta_1 + \delta_2)/2$  is the average (common-mode) laser detuning,  $d_{mn}$  represents the normalized dipole matrix element corresponding to the  $(m \rightarrow n)$  transition,  $\Omega_1$  ( $\Omega_2$ ) is the Rabi frequency of the CPT field at frequency  $\omega_1$  ( $\omega_2$ ) corresponding to a transition with a normalized dipole matrix element value of unity, and  $h.c.$  stands for Hermitian conjugate. The coupling terms involving  $\Omega_1$  (fourth term, to be denoted as  $H_A^{(4)}$ ) and  $\Omega_2$  (fifth term, to be denoted as  $H_A^{(5)}$ ) in equation (1) include  $\sigma^+$  and  $\sigma^-$  circular transitions, with the values of the normalized matrix elements depending on the polarization states of the CPT fields. For example, if the CPT fields have  $\hat{x}$ -polarized (lin || lin) polarization states, the coupling terms in equation (1) have the following form:

$$H_A^{(4)} = \frac{\Omega_1}{2} \left( -\frac{1}{\sqrt{12}}(s_{2,9} + s_{3,10} + s_{3,14}) - \frac{1}{\sqrt{4}}s_{2,13} - \frac{1}{\sqrt{2}}s_{1,12} \right) + \frac{\Omega_1}{2} \left( \frac{1}{\sqrt{12}}(s_{1,10} + s_{2,11} - s_{1,14}) - \frac{1}{\sqrt{4}}s_{2,15} - \frac{1}{\sqrt{2}}s_{3,16} \right) \quad (2)$$

$$H_A^{(5)} = \frac{\Omega_2}{2} \left( \frac{1}{\sqrt{12}}s_{6,9} + \frac{1}{\sqrt{6}}(s_{5,12} + s_{8,15}) + \frac{1}{\sqrt{4}}(s_{7,10} + s_{6,13} + s_{7,14}) + \frac{1}{\sqrt{2}}s_{8,11} \right) + \frac{\Omega_2}{2} \left( \frac{1}{\sqrt{12}}s_{6,11} + \frac{1}{\sqrt{6}}(-s_{4,13} - s_{7,16}) + \frac{1}{\sqrt{4}}(s_{5,10} - s_{5,14} - s_{6,15}) + \frac{1}{\sqrt{2}}s_{4,9} \right) \quad (3)$$

The terms in equations (2) and (3) contain a sum of all  $\sigma^+$  transitions (the first bracketed term) and  $\sigma^-$  transitions (the second bracketed term). Similarly, we formulated the coupling terms for other polarization states corresponding to only  $(\sigma^+, \sigma^+)$  or  $(\sigma^-, \sigma^-)$  and lin  $\perp$  lin schemes. The Hamiltonian  $H_B$  for the sixteen-level system is defined as

$$H_B = B_z [A_1(s_{1,1} - s_{3,3}) + A_2(2s_{4,4} + s_{5,5} - s_{7,7} - 2s_{8,8}) + A_3(s_{9,9} - s_{11,11}) + A_4(2s_{12,12} + s_{13,13} - s_{15,15} - 2s_{16,16})] + B_z^2 [Q_0(s_{2,2} + s_{6,6}) + Q_1(s_{1,1} + s_{3,3} + s_{5,5} + s_{7,7})] + \left\{ B_T \left[ \frac{A_1}{\sqrt{2}}(s_{2,1} + s_{3,2}) + A_2 \left( s_{5,4} + \frac{\sqrt{6}}{2}(s_{6,5} + s_{7,6}) + s_{8,7} \right) \right] + \frac{A_3}{\sqrt{2}}(s_{10,9} + s_{11,10}) + A_4 \left( s_{13,12} + \frac{\sqrt{6}}{2}(s_{14,13} + s_{15,14}) + s_{16,15} \right) \right\} + h.c. \quad (4)$$

where  $B_z$  corresponds to the longitudinal (or axial) magnetic field (LMF) along the quantization axis, which is chosen to be

the  $z$ -direction and coincides with the direction of propagation of the laser beams,  $B_x$  ( $B_y$ ) represents a magnetic field along the  $x$  ( $y$ ) direction, and we have defined  $B_T = B_x + iB_y$  as the transverse magnetic field (TMF). The parameters  $A_q = g_q \mu_B / \hbar$  ( $q = 1, 2, 3, 4$ ) in equation (4) correspond to linear Zeeman shift coefficients of  $|F = 1\rangle$ ,  $|F = 2\rangle$ ,  $|F' = 1\rangle$  and  $|F' = 2\rangle$  states, respectively, with  $g_q = \left( \frac{5g_l - g_r}{4}, \frac{3g_l + g_r}{4}, \frac{5g_l - g_r}{4}, \frac{3g_l + g_r}{4} \right) = (-0.5017, 0.4997, -0.1677, 0.1657)$  being the effective Landé  $g$ -factors and  $\mu_B$  being the Bohr magneton. The numerical values  $A_q$  are  $(-0.7022, 0.6994, -0.2347, 0.2319)$  MHz/G. A TMF can be produced, for example, by a small angular misalignment between the applied LMF and the direction of optical beam propagation in the cell. In addition to a TMF, our model also incorporates the Breit-Rabi equation [17, 18, 36] to include LMF induced quadratic Zeeman shifts of  $m_F$  sublevels in  $|F = 1\rangle$  and  $|F = 2\rangle$  states. The parameters  $Q_k = \frac{(g_l - g_r)^2(4 - m_F^2)\mu_B^2}{16 \hbar^2 \omega_{\text{hf}}}$  ( $k = 0, 1$ ) in equation (4) correspond to quadratic Zeeman shift coefficients with  $k = 0$  corresponding to  $m_F = 0$  sublevel and  $k = 1$  corresponding to  $m_F = \pm 1$  sublevels, for both  $|F = 1\rangle$  and  $|F = 2\rangle$  states. The coefficient  $Q_2$  for  $m_F = \pm 2$  is zero. The numerical values of  $Q_k$  are  $(286.57, 215.68)$  Hz/G<sup>2</sup>. We account for the decay of atomic levels by defining  $H_T$  as [35]

$$H_T = -\frac{i}{2} \left( \sum_{m=1}^3 \gamma_1 s_{m,m} + \sum_{m=4}^8 \gamma_2 s_{m,m} + \sum_{m=9}^{16} \Gamma s_{m,m} \right) \quad (5)$$

where  $\Gamma$  is the total decay rate from each sublevel in the excited states  $|F' = 1, 2\rangle$ , and  $\gamma_1$  and  $\gamma_2$  are the effective decay rates for the ground states  $|F = 1\rangle$  and  $|F = 2\rangle$ , respectively. The source matrix  $L$  in the density-matrix equation contains non-zero diagonal elements that account for the influx of atoms decaying from other states:

$$L = \Gamma \sum_{m=1}^8 s_{m,m} \sum_{n=9}^{16} d_{nm}^2 \rho_{nn} + \frac{\gamma_2}{3} \sum_{m=1}^3 s_{m,m} \sum_{n=4}^8 \rho_{nn} + \frac{\gamma_1}{5} \sum_{m=4}^8 s_{m,m} \sum_{n=1}^3 \rho_{nn} \quad (6)$$

Here,  $d_{nm}^2$  represents the square of the normalized matrix element for the  $(n \rightarrow m)$  decay channel. The source matrix  $L$  includes the ground state population influx due to all possible decay channels corresponding to  $\sigma^+$ ,  $\sigma^-$ , and  $\pi$  transitions, as well as the population exchange between the ground states. A system of linear and time-dependent equations for the density-matrix elements  $\rho_{mn}$  are obtained by using  $H$  and  $L$  matrices given by equations (1)–(5) in the Liouville equation described previously. This system of equations is recast as a vector-matrix equation [35] in the form  $\frac{d}{dt} \vec{\rho} = M \vec{\rho}$ , where  $\vec{\rho}$  is a vector consisting of 256 elements  $\rho_{mn}$  and  $M$  is a  $(256 \times 256)$

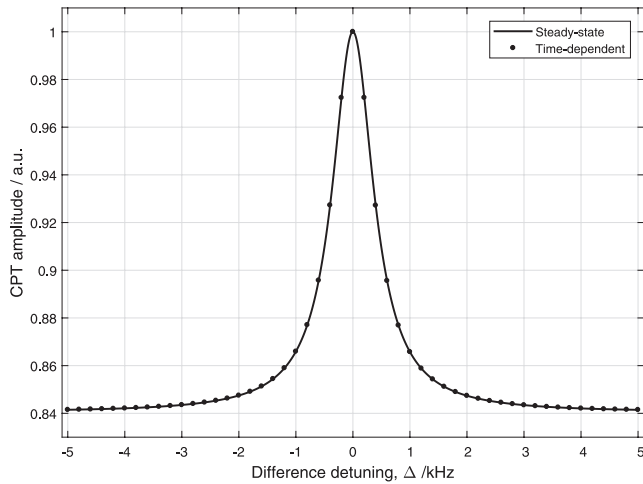


**Figure 2.** Calculated velocity-averaged CPT resonance showing a close match between the steady-state and time-dependent solutions. We considered  $\hat{x}$ -polarized lin || lin excitation resonant with the  $|F' = 1\rangle$  state and used the following parameters in our calculation:  $B_z = 5$  mG,  $\Omega_1 = \Omega_2 = \Gamma/60$ ,  $\Gamma = 6$  MHz, and  $\gamma_1 = \gamma_2 = 200$  Hz.

matrix consisting of the coefficients of  $\rho_{mn}$  gathered from the Liouville equation. We developed a computational model to find time-dependent as well as steady-state solutions for  $\rho_{mn}$  for studying CPT using different polarization schemes. Under the steady-state condition, the solutions for  $\vec{\rho}$  are obtained by equating  $\frac{d}{dt}\vec{\rho}$  to zero, reducing  $M$  to a matrix  $W$  of reduced dimension ( $255 \times 255$ ) using the condition  $\sum_{m=1}^{16} \rho_{mm} = 1$  for a closed atomic system [35], and finding  $W^{-1}$ . The time-dependent solutions for  $\vec{\rho}$  are obtained from the eigenvalues and eigenvectors of the  $M$  matrix. The CPT spectrum is obtained by finding  $\vec{\rho}$  as a function of the difference detuning  $\Delta$  between the CPT fields. Velocity averaging is also performed to account for the atomic motion in the vapor medium. This is achieved by modifying the single-photon detuning terms in the Hamiltonian in equation (1) as  $\delta'_{1,2} = \delta_{1,2} \pm \omega_{1,2}(v/c)$  for the individual velocity group,  $v$ , and performing a weighted-average of the CPT spectrum calculated for individual  $v$ , via integration over the Maxwell–Boltzmann velocity distribution,  $(1/\sqrt{2\pi}v_p)\exp(-v^2/v_p^2)$ , where  $v_p = \sqrt{2k_B T/m}$  is the most probable velocity corresponding to atomic mass  $m$ , sample temperature  $T$ , and  $k_B$  is the Boltzmann constant.

Figure 2 shows the velocity-averaged CPT resonance produced around  $\Delta = 0$ , represented by the sum of the populations in states 9 through 16 (i.e.  $\sum_{m=9}^{16} \rho_{mm}$ ), using steady-state as well as time-dependent solutions, for excitation using  $\hat{x}$ -polarized lin || lin CPT fields. The CPT fields were chosen to be resonant with the  $|F' = 1\rangle$  state. For this simulation, we have used parameters which correspond to  $\Omega_1 = \Omega_2 = \Omega \equiv \sqrt{(|\Omega_1|^2 + |\Omega_2|^2)}/2 = \Gamma/60$ . For an ideal three-level system, with the Rabi frequency for leg one being  $\Omega_1 \ll \Gamma$  and that for the leg two being  $\Omega_2 \ll \Gamma$ , the linewidth of the CPT signal is expected to be  $\sim(\gamma + \Omega^2/\Gamma)$  [37], where  $\gamma = (\gamma_1 + \gamma_2)/2$ . For  $\Gamma = 6$  MHz and  $\gamma_1 = \gamma_2 = \gamma = 200$  Hz,

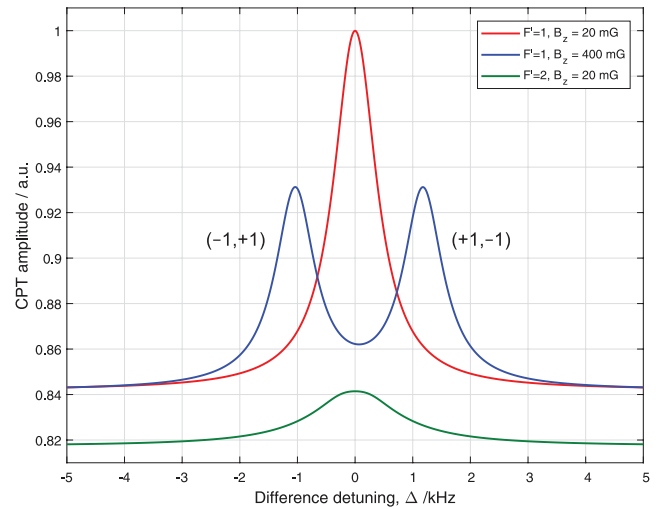


**Figure 3.** Splitting of the central CPT resonance formed by lin || lin excitation at higher axial magnetic field. The following parameters were used in our calculation:  $\Omega_1 = \Omega_2 = \Gamma/60$ ,  $\Gamma = 6$  MHz, and  $\gamma_1 = \gamma_2 = 200$  Hz.

the linewidth for an ideal CPT system would be  $\sim 1.9$  kHz. The linewidth in figure 2 is seen to be somewhat smaller:  $\sim 0.9$  kHz. This is due to several factors. First, note that we have defined  $\Omega_1$  and  $\Omega_2$  to be Rabi frequencies corresponding to transitions with normalized matrix elements of unity values. However, the actual matrix elements involved are significantly smaller. Second, the fields are detuned with respect to the  $|F' = 2\rangle$  state; the linewidth of a CPT resonance decreases when the excitation is detuned with respect to the intermediate state. Third, because of the velocity spread, most atoms are detuned away from optical resonance.

It should be noted that the solutions obtained from the steady-state and time-dependent models show an excellent match in figure 2. A near steady-state solution is obtained from the time-dependent model by considering temporal Raman excitation with a long CPT pulse ( $\tau = 2$  ms). The time-dependent model is particularly suitable for studying the dark-state CPT resonance under non-steady state conditions and simulating pulsed CPT excitation which produces Raman–Ramsey interference [34, 38].

### 2.1. Investigation of different optical excitation schemes

The sixteen-level steady-state model is further used to investigate CPT spectra and resonances produced by different optical excitation schemes. The goal of this study is to determine which of the three cases to be considered would be best suited for a compact CPT rubidium clock. We first considered the lin || lin polarization scheme, which can be created by a single, linearly polarized, modulated laser beam via a vertical-cavity surface emitting laser (VCSEL) or an electro-optic modulator (EOM).

For simulating excitations using linearly polarized CPT fields, coupling terms for both  $\sigma^+$  and  $\sigma^-$  transitions with proper relative phase are included in  $H_A$  in equation (1). Figure 3 shows the CPT resonance produced by lin || lin around  $\Delta = 0$

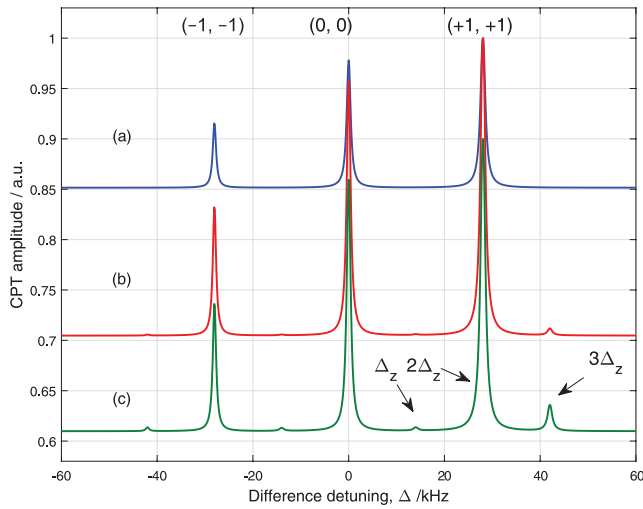


**Figure 4.** CPT spectrum generated by  $(\sigma^+, \sigma^+)$  polarized light resonant with the  $|F' = 2\rangle$  state. The result shows Zeeman CPT resonances formed by the vector magnetic field  $\vec{B}$  used in our calculation with its magnitude  $B = 20$  mG and angle (a)  $0^\circ$  (b)  $5^\circ$  (c)  $10^\circ$  with respect to the direction of beam propagation in the cell. For the purpose of illustration, the CPT amplitudes in (b) and (c) are doubled and (c) is vertically offset by subtracting 0.1 from it, to show more clearly the small CPT resonances formed by the TMF component of  $\vec{B}$ . The following parameters were used in our calculation:  $\Omega_1 = \Omega_2 = \Gamma/60$ ,  $\Gamma = 6$  MHz, and  $\gamma_1 = \gamma_2 = 200$  Hz.

for  $B_z = 20$  mG and 400 mG, for resonant excitation with the  $|F' = 1\rangle$  excited state, and for  $B_z = 20$  mG for resonant excitation with the  $|F' = 2\rangle$  excited state. Such a scheme automatically prevents the formation of trap states due to the simultaneous presence of  $\sigma^+$  and  $\sigma^-$  excitations. The population decay rates for the ground states are taken to be  $\gamma_1 = \gamma_2 = 200$  Hz in this case; non-vanishing values of these rates are necessary for preventing trap states, as in the case for  $\sigma^+$  or  $\sigma^-$  excitations, to be discussed later, however they are included for comparison here.

For resonant excitation with the  $|F' = 1\rangle$  excited state, the splitting of the central CPT resonance in figure 3 exhibits high sensitivity to  $B_z$  compared to the typical CPT resonance produced by the dark state from a pair of  $m_F = 0$  sublevels in  $|F = 1\rangle$  and  $|F = 2\rangle$  ground states. This can be explained as follows: dark states for lin || lin excitation are produced from a pair of ground-state sublevels  $|F = 1, m_F = -1\rangle$ ,  $|F = 2, m_F = +1\rangle$  and  $|F = 1, m_F = +1\rangle$ ,  $|F = 2, m_F = -1\rangle$ , and are described by [19]

$$\left| \text{Dark}_{\begin{pmatrix} -1, +1 \\ +1, -1 \end{pmatrix}} \right\rangle = C_{\pm} \left[ |F = 1, m_F = \mp 1\rangle - \frac{d_{\sigma_{\pm}}^{(1)} E_{\sigma_{\mp}}^{(1)}}{d_{\sigma_{\mp}}^{(2)} E_{\sigma_{\pm}}^{(2)}} |F = 2, m_F = \pm 1\rangle \right] \quad (7)$$

where  $d_{\sigma_{\pm}}^{(1,2)}$  are  $\sigma^+$  and  $\sigma^-$  elements of the dipole operator,  $E_{\sigma_{\pm}}^{(1,2)}$  are circularly polarized components of the CPT fields, and  $C_{\pm}$  are normalization constants.

The two dark states in equation (7) have a linear magnetic field sensitivity arising from the nuclear spin  $g$ -factor,  $g_I$ , which gives rise to high magnetic field splitting in the presence of  $B_z$ . The magnetic field dependencies of the  $(-1, +1)$  and  $(+1, -1)$  dark states are experimentally measured and discussed later. It is also important to note that a 0–0 dark state cannot be formed in the ground-states  $|F = 1, m_F = 0\rangle$  and  $|F = 2, m_F = 0\rangle$  by lin || lin excitation, because of differing signs of the relevant dipole matrix elements. High magnetic field sensitivity of lin || lin polarization can limit the mid- or long-term frequency stability of the atomic clock. For two-photon excitation resonant with  $|F' = 2\rangle$  state, the CPT resonance produced by lin || lin polarization is shown to have a much lower contrast. In this case, states described in equation (7) are dark with respect to the  $|F' = 1\rangle$  state, as well as the  $|F' = 2, m_F = 0\rangle$  state, but see non-vanishing excitations to  $|F' = 2, m_F = \pm 2\rangle$  states.

The polarization scheme often used in a CPT clock comprise  $(\sigma^+, \sigma^+)$  or  $(\sigma^-, \sigma^-)$  circularly polarized light. The model allows us to simulate and investigate characteristics of CPT spectral resonances for different cases: resonant excitations with  $(\sigma^+, \sigma^+)$  or  $(\sigma^-, \sigma^-)$  polarized fields with  $|F' = 1\rangle$  or  $|F' = 2\rangle$  excited states. Figure 4 shows the CPT spectrum generated by  $(\sigma^+, \sigma^+)$  polarized light for  $B_z = 20$  mG and resonant excitation with  $|F' = 2\rangle$ . The population decay rates for the ground states are taken to be  $\gamma_1 = \gamma_2 = 200$  Hz; non-vanishing values of these parameters must be used in this case in order to prevent trapping of atoms in the extremal Zeeman sublevels. In addition to the central CPT resonance at  $\Delta = 0$ , strong  $(-1, -1)$  and  $(+1, +1)$  Zeeman CPT resonances are formed at  $\Delta = \pm 2\Delta_z$ , where  $\Delta_z \equiv g_F \mu_B B_z$ , by a pair of Zeeman-shifted ground-state sublevels  $|F = 1, m_F = -1\rangle$ ,  $|F = 2, m_F = -1\rangle$  and  $|F = 1, m_F = +1\rangle$ ,  $|F = 2, m_F = +1\rangle$ . Being closer to the  $|F = 2, m_F = +2\rangle$  trap state, the  $(+1, +1)$  Zeeman states have higher atomic populations; therefore, the  $(+1, +1)$  CPT resonance in figure 4 has higher contrast. The resonance at  $\Delta = 0$  is produced by the 0–0 clock state resulting from a single  $\Lambda$ -transition from  $|F = 1, m_F = 0\rangle$ ,  $|F = 2, m_F = 0\rangle$  to  $|F' = 2, m_F = +1\rangle$ , which is viable for clock applications, since the 0–0 CPT resonance is insensitive to magnetic fields to first-order. The presence of these additional resonances reduces the contrast of the 0–0 resonance.

Results in figure 4 also show the effect of TMF on the CPT spectrum generated by the  $(\sigma^+, \sigma^+)$  polarized light. Unintentional but small misalignment of the cell axis with respect to the applied LMF can produce TMF in the cell environment. The result shows that new CPT resonances are generated at  $\Delta = \pm \Delta_z$ ,  $\pm 3\Delta_z$  in the presence of TMF. The TMF gives rise to population redistribution among the Zeeman sublevels, resulting in new  $\Lambda$  sub-systems formed by effective  $\pi$ -transitions between the ground- and excited-state sublevels [39, 40]. Thus, the contrast in the central CPT resonance is further reduced.

One of the preferred polarization schemes for producing high contrast CPT resonances in the 0–0 clock state is lin  $\perp$  lin

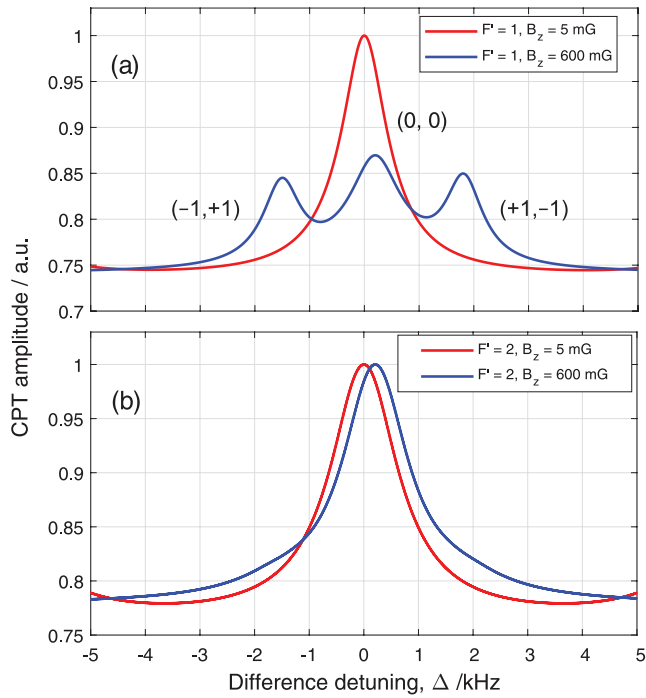


**Figure 5.** Splitting of the central CPT resonance formed by  $\text{lin} \perp \text{lin}$  excitation resonant with (a)  $|F' = 1\rangle$  state, and (b)  $|F' = 2\rangle$  state at higher axial magnetic field. The following parameters were used in our calculation:  $\Omega_1 = \Omega_2 = \Gamma/60$ ,  $\Gamma = 6$  MHz, and  $\gamma_1 = \gamma_2 = 200$  Hz.

where two linear and orthogonal polarizations make up the CPT fields. Such a scheme (as well as the  $\text{lin} \parallel \text{lin}$  scheme, as mentioned earlier) automatically prevents the formation of trap states due to the simultaneous presence of  $\sigma^+$  and  $\sigma^-$  excitations. In practice,  $\text{lin} \perp \text{lin}$  cannot be directly created from a single, modulated laser beam used in the CPT clock. An alternative method known as PPOP using the modulated laser beam in a polarization-based Michelson interferometer [23] can substitute for  $\text{lin} \perp \text{lin}$ . Using a simple analysis of the CPT fields in the modulated laser beam, we have shown in section 3 that this method is equivalent to  $\text{lin} \perp \text{lin}$  excitation [24]. Figure 5 shows the calculated CPT resonance at  $\Delta = 0$  using our model for the  $\text{lin} \perp \text{lin}$  excitation.

In this case, we observed a noticeable difference in CPT characteristics between resonant two-photon excitations with  $|F' = 1\rangle$  and  $|F' = 2\rangle$  states. For a vanishingly small magnetic field ( $B_z = 5$  mG), the central CPT resonance in figure 5(a) for resonant  $|F' = 1\rangle$  is due to all three dark states: (0, 0), (-1, +1) and (+1, -1). However, these dark states produce separated CPT resonances when a significant magnetic field is applied ( $B_z = 600$  mG in this case). In contrast, the central CPT resonance in figure 5(b) for resonant  $|F' = 2\rangle$  is mainly due to the (0, 0) dark state, since the (-1, +1) and (+1, -1) ‘dark states’ are not fully dark in this case due to coupling to additional Zeeman sublevels in the  $|F' = 2\rangle$  state. This is confirmed by using  $B_z = 600$  mG which produces a single CPT resonance in figure 5(b) exhibiting the second-order magnetic

field sensitivity of the 0–0 dark state; the contributions from the (-1, +1) and (+1, -1) ‘quasi dark states’ appear as small bumps.

### 3. Experiment

The diagram in figure 6 depicts the experimental setup used in investigating CPT characteristics by employing the polarization schemes described above. The setup is also used as a CPT clock to measure the frequency stability for each scheme. A tunable diode laser (DL PRO, Toptica Photonics) with line-width less than 1 MHz is used as the light source. A pure-isotope  $^{87}\text{Rb}$  vapor cell (length = 2 cm, diameter = 1 cm), filled with 10 Torr neon buffer gas (Triad Technology, Inc.) is used in our experiment. The laser beam is sent through a fiber-coupled waveguide electro-optic modulator (EOM, EOSpace AZ-0S5-10-PFA-PFA-795, bias  $V_\pi = 1.4$  V) driven by an RF oscillator to produce the frequency-modulated laser beam for CPT experiments. The EOM is driven by approximately 20 dBm RF power to produce optical sidebands around the laser carrier frequency. The difference in frequency between the first two sidebands is matched close to 6.834 GHz, the hyperfine ground-state frequency of  $^{87}\text{Rb}$ , fine-tuned to account for the buffer gas pressure induced frequency shift ( $\Delta f_{\text{buf}} = 3.022$  kHz) in the cell.

During the experiment, the laser frequency is locked to the Doppler-broadened  $^{87}\text{Rb}$  D1 absorption maximum created by resonant excitation of the modulated laser beam [11, 41]. This allows us to use a single photodetector for implementing the laser lock as well as the CPT clock. The laser lock is implemented via dither modulation and a laser servo controller shown in figure 6. The dither modulation frequencies for the laser servo and the clock servo, which operate independently, are chosen to be unequal in order to prevent lock instability caused by interference.

The EOM has an undesirable temperature dependence of its bias voltage. Since the bias voltage controls the optical power in the carrier and the sidebands, any temperature drift due to internal heating causes appreciable drift in power in the carrier and the sidebands. The off-resonant carrier also contributes to the CPT background which reduces the contrast in the CPT signal. We actively control the EOM bias voltage to minimize the carrier power. This is done by picking off a small fraction of the beam after the EOM, measuring it with a photodiode and implementing an electronic servo by deriving a correction signal from the dithered EOM bias voltage [42]. In addition, an active thermal control of the EOM using a TEC (thermo-electric cooler) and a temperature controller is used to further minimize the drift in the EOM bias voltage. Residual drift in the carrier (or sideband) power is also monitored with a scanning Fabry–Perot etalon (not shown in the figure). The RF signal at ~3.4 GHz for driving the EOM is synthesized from a 10 MHz temperature-stabilized voltage controlled oscillator (TSVCO, 501-04609A, Wenzel) using a fractional phase-locked loop (Frac-N PLL, LMX2487E, Texas Instruments). The PLL output is internally connected to the on-board 3.417 GHz oscillator via an integrating servo

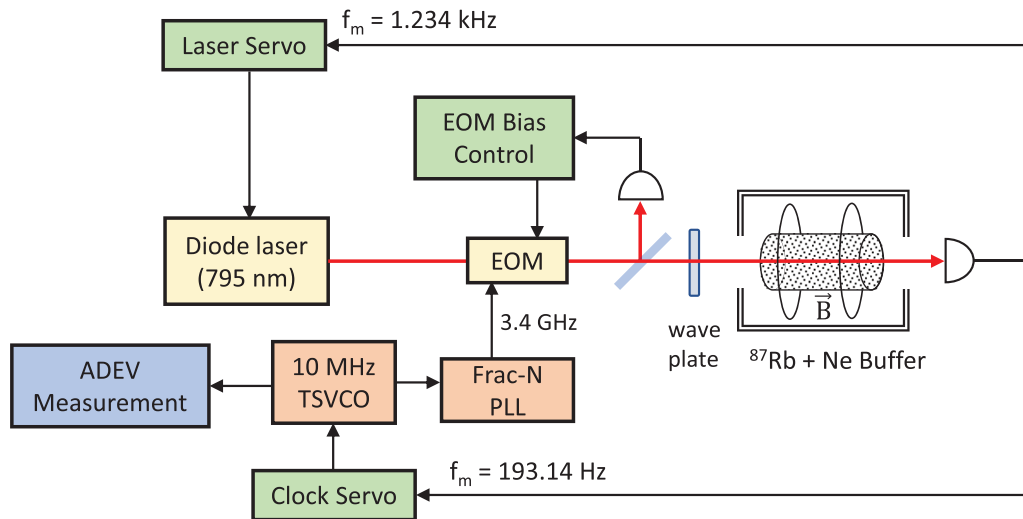


**Figure 6.** Experimental setup developed for the rubidium CPT clock. A single photodetector distributes the optical signal and produces independent control signals for the laser servo and the clock servo. The waveplate is either  $\lambda/2$  or  $\lambda/4$ , for implementing  $\text{lin} \parallel \text{lin}$  or  $(\sigma, \sigma)$  polarization schemes.

(or loop filter) which locks the RF in phase with the master 10 MHz TSVCO. This way, any change to the 10 MHz TSVCO results in a proportional change to the RF and hence, the laser modulation frequency.

The physics package of the vapor cell has an approximate cylindrical volume of 7000 cubic cm which comprise a dual layer  $\mu$ -metal magnetic shield enclosure surrounding the cell to mitigate residual magnetic fields by approximately 40 dB. We use a pair of Helmholtz coils (diameter = 16.5 cm) mounted inside the enclosure to apply a small uniform axial magnetic field ( $B \approx 30$  mG) for lifting the Zeeman degeneracies of the  $^{87}\text{Rb}$  atomic states. The rubidium cell is actively temperature controlled ( $\Delta T \approx 100$  mK) with bifilar-twisted resistive nichrome heating wire and a standard K-type thermocouple sensor. In order to find the optimal cell temperature, we measured the contrast of the CPT signal generated with  $(\sigma^-, \sigma^-)$  excitation, by varying the cell temperature. Figure 7 shows CPT contrast plotted as a function of the cell temperature. Thus, for all our studies, the cell is actively maintained at a steady and optimal temperature of 53 °C where the contrast is found to be close to its maximum. The laser beam emerging from the EOM is expanded using a fiber-end collimator to an approximate diameter of 8 mm before passing it through the rubidium cell. A combination of the expanded beam size and frequent collisions of  $^{87}\text{Rb}$  atoms with buffer gas atoms increase the interaction time between the laser fields and  $^{87}\text{Rb}$  atoms for observing narrow linewidth CPT resonance. Sub-kilohertz linewidth CPT resonance, limited by the optical power, is observed by scanning the laser modulation frequency (sweeping the TSVCO) around the two-photon resonant condition.

The polarization states for the CPT excitation fields are controlled using a wave plate in the beam path. In the case of  $\text{lin} \parallel \text{lin}$  excitation, a properly oriented half-wave ( $\lambda/2$ ) plate establishes a particular linear polarization state. To choose  $(\sigma, \sigma)$  excitation, the  $\lambda/2$  plate is replaced by a quarter-wave ( $\lambda/4$ ) plate. However, to employ  $\text{lin} \perp \text{lin}$  (or PPOP),

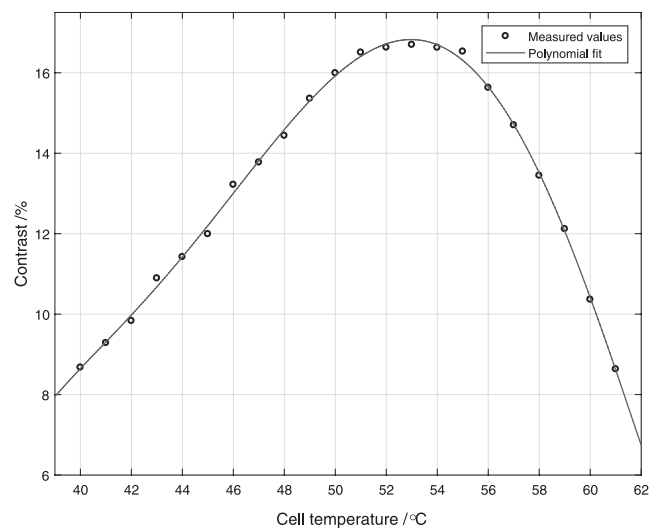


**Figure 7.** CPT contrast measured by varying the cell temperature from 40 °C to 61 °C in steps of 1 °C under the temperature lock condition.

a polarization-based Michelson interferometer (schematic shown in figure 8) is used in the beam path. Each arm of the interferometer consists of a  $\lambda/4$  plate and a retro-reflecting mirror. The  $\lambda/4$  plates change the beam polarization from linear to circular during the forward pass, and from circular to an orthogonal linear polarization during the return. The beams are combined at the polarizing beam splitter (PBS) and emerge with orthogonal horizontal and vertical linear polarization states from the two arms of the interferometer. Finally, a  $\lambda/4$  plate at the output of the interferometer converts the modulated laser beams to right circular polarization (RCP) for one arm and left circular polarization (LCP) for the other. One of the interferometer arms is changed to set the path difference between the two arms by one quarter of a wavelength  $\lambda_{\text{hf}}$  corresponding to the  $^{87}\text{Rb}$  hyperfine ground state frequency 6.834 GHz. This is approximately 1.1 cm. Since the beam travels twice along the interferometer arm, the overall

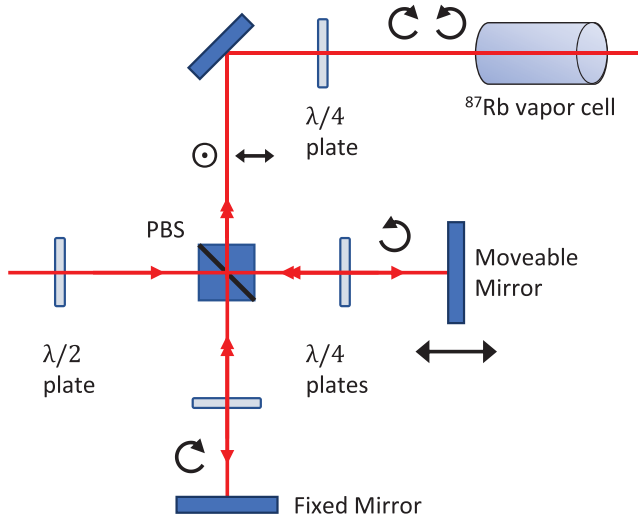


**Figure 8.** Schematic of the polarization-based Michelson interferometer introduced in the beam path shown in figure 6 for implementing  $\text{lin} \perp \text{lin}$  (or PPOP) scheme. The path difference between the two arms of the interferometer is set to  $\lambda_{\text{hf}}/4$  which is approximately 1.1 cm for  $^{87}\text{Rb}$  atoms.

path difference is  $\lambda_{\text{hf}}/2$ . This ensures that the modulated laser beams emerging from the interferometer have a  $90^\circ$  phase difference with their electric fields after the  $\lambda/4$  plate. This can be described as follows:

$$\vec{E}_{\text{CPT}}^{(1)} = 2E_0 \cos\left(\frac{k_1 - k_2}{2}z_1 - \frac{\omega_1 - \omega_2}{2}t\right) \times [\hat{x} \cos(\bar{k}z_1 - \bar{\omega}t) + \hat{y} \sin(\bar{k}z_1 - \bar{\omega}t)] \quad (8a)$$

$$\vec{E}_{\text{CPT}}^{(2)} = 2E_0 \sin\left(\frac{k_1 - k_2}{2}z_1 - \frac{\omega_1 - \omega_2}{2}t\right) \times [\hat{x} \cos(\bar{k}z_2 - \bar{\omega}t) - \hat{y} \sin(\bar{k}z_2 - \bar{\omega}t)] \quad (8b)$$

where  $\bar{k} = (k_1 + k_2)/2$  and  $\bar{\omega} = (\omega_1 + \omega_2)/2$  are average values of the propagation constant and angular frequency of the modulated laser beam, respectively. Equal amplitude  $E_0$  has been considered for the RCP and LCP fields. Equation (8) shows that the CPT beams have orthogonal circular polarizations and their amplitudes oscillate at half the  $^{87}\text{Rb}$  hyperfine frequency  $\nu_{\text{hf}}$  with a quadrature phase difference. Thus, when the intensity (time-averaged) of RCP (or  $\sigma^+$ ) beam is maximum, the intensity of LCP (or  $\sigma^-$ ) beam is zero and vice versa. This produces alternate excitations and optical pumping using  $\sigma^+$  and  $\sigma^-$  polarization states, which is known as PPOP that gives rise to high contrast in the CPT signal [23, 24]. One can also show the equivalence between PPOP and  $\text{lin} \perp \text{lin}$  [24] by superposing the modulated laser fields (sidebands) together in equation (8) to obtain

$$\vec{E}_{\text{T}} = \vec{E}_{\text{CPT}}^{(1)} + \vec{E}_{\text{CPT}}^{(2)} = 2E_0 [\{\hat{x} \cos \theta + \hat{y} \sin \theta\} \cos(k_1 z' - \omega_1 t) + \{\hat{x} \sin \theta - \hat{y} \cos \theta\} \cos(k_2 z' - \omega_2 t)] \quad (9)$$

where  $z' = (z_1 + z_2)/2$  is the average distance and  $\theta = k_1|z_1 - z_2|/2 = k_1(\lambda_{\text{hf}}/4)$  that corresponds to the angle of the linear polarization state of the electric field at frequency  $\omega_1$  and  $\omega_2$ . The curly bracketed terms in equation (9) represent

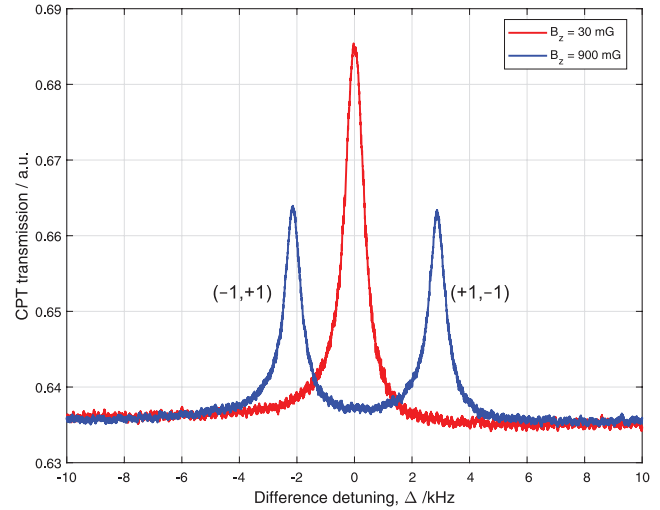


**Figure 9.** Magnetic field induced splitting of the central CPT resonance (linewidth = 841 Hz, contrast = 7.5%) generated by  $\text{lin} \parallel \text{lin}$  excitation resonant with  $|F' = 1\rangle$  state.

the two orthogonal linear polarization CPT fields ( $\text{lin} \perp \text{lin}$ ) at frequencies  $\omega_1$  and  $\omega_2$ , respectively. Thus, the  $\text{lin} \perp \text{lin}$  excitation scheme discussed in section 2.1 is realized using the polarization interferometer shown in figure 8. The  $\text{lin} \perp \text{lin}$  excitation scheme can also be implemented without the polarization interferometer by using counter-propagating  $\sigma^+$  and  $\sigma^-$  polarized modulated laser beams through a cell [22, 43]. In this case, one can show

$$\begin{aligned} \vec{E}_{\text{T}} &= \vec{E}_{\text{CPT}}^{(\sigma^+, +z)} + \vec{E}_{\text{CPT}}^{(\sigma^-, -z)} \\ &= 2E_0 [\{\hat{x} \cos \theta_1 + \hat{y} \sin \theta_1\} \cos(\theta - \omega_1 t) \\ &\quad - \{\hat{x} \sin(\theta_1 - \theta'(z_1)) + \hat{y} \cos(\theta_1 - \theta'(z_1))\} \sin(\theta - \omega_2 t)] \end{aligned} \quad (10)$$

where  $\theta_1 = k_1(z_1 + z_2)/2$  corresponds to the angle of the linear polarization state at frequency  $\omega_1$ . The curly bracketed terms in equation (10) show two linear polarization states with standing wave fields at frequencies  $\omega_1$  and  $\omega_2$  which are orthogonal provided  $\theta'(z_1) = 2\pi z_1/\lambda_{\text{hf}}$  is an integer multiple of  $\pi$  for a particular location  $z_1$  inside the cell. If orthogonality is satisfied at  $z_1$ , it will not be strictly satisfied at other locations inside the cell for which  $z_1$  deviates by a distance  $\ll \lambda_{\text{hf}}/4$  ( $\approx 1.1$  cm). Thus,  $\text{lin} \perp \text{lin}$  excitation scheme cannot be implemented with counter-propagating  $\sigma^+$  and  $\sigma^-$  beams in relatively long cells, like ours, which is 2 cm long. For atoms with significant Doppler broadening, this approach will also cause a significant reduction in signal. As such, this scheme is more suitable for microcells with cold atoms [22, 43].

#### 4. Experimental results and discussions

We prepared the modulated laser beam in the  $\text{lin} \parallel \text{lin}$  polarization state, and measured the characteristics of CPT resonance. Figure 9 shows the central CPT resonance observed with  $\text{lin} \parallel \text{lin}$  excitation resonant with the  $|F' = 1\rangle$  state for

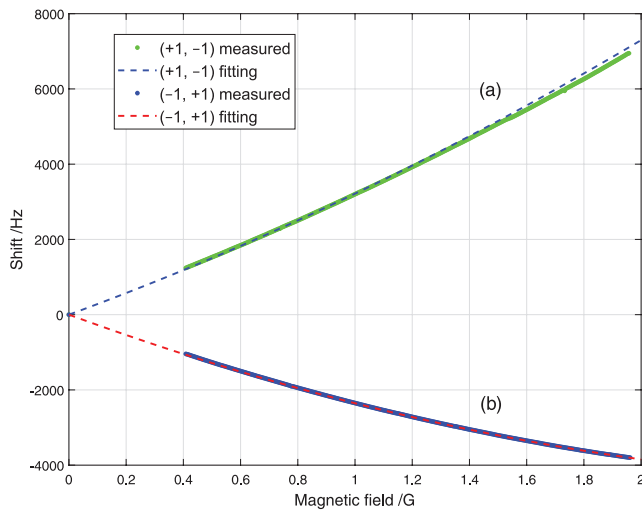


**Figure 10.** Magnetic field dependencies of (a) the  $(+1, -1)$  CPT resonance, shown in right in figure 9 and (b) the  $(-1, +1)$  CPT resonance, shown in left in figure 9. The dashed lines represent the fittings obtained using the Breit-Rabi equation.

two different axial magnetic field strengths. With low axial magnetic field ( $B_z \simeq 30$  mG), a single-peaked CPT resonance with linewidth of 841 Hz and contrast of 7.5% is observed. CPT contrast is measured by calculating  $(V_P - V_B)/V_P$  where  $V_P$  and  $V_B$  are defined as the respective peak and background voltage levels of the CPT signal [27]. The total optical power used in the modulated laser beam was approximately 70  $\mu$ W. At higher magnetic field ( $B_z \simeq 900$  mG), the CPT resonance is split into two separate resonances. This is consistent with our simulated result shown for  $\text{lin} \parallel \text{lin}$  excitation in figure 3.

The central CPT resonance consists of two dark states formed by  $(-1, +1)$  and  $(+1, -1)$  ground state  $m_F$  sublevels in  $^{87}\text{Rb}$ . These dark states have higher magnetic field sensitivity than the conventional  $0-0$  dark state. Figure 10 shows the magnetic field dependencies of  $(-1, +1)$  and  $(+1, -1)$  CPT resonances produced by the  $\text{lin} \parallel \text{lin}$  scheme. These measurements are obtained by slowly changing the current in the Helmholtz coil while keeping the laser modulation frequency locked to the peak of CPT resonance using an electronic servo, and measuring the shift in the modulation frequency with a frequency counter. Our measurements could only be taken when the  $(-1, +1)$  and  $(+1, -1)$  resonances were separated by  $B_z$  sufficiently enough to allow the servo to lock. The two resonances split asymmetrically as  $B_z$  is gradually increased. As expected, the splitting also exhibits a nonlinear dependence on  $B_z$ . The experimental trends agree very well with the magnetic field dependencies shown in dashed lines in figure 10 as theoretical fittings obtained from the Breit-Rabi equation [17, 18]:

$$\Delta_{\substack{(+1,-1) \\ (-1,+1)}} = \omega_{\text{hf}} \pm \left( \frac{2g_I \mu_B}{\hbar} \right) B_z + \left( \frac{3}{4} \frac{(g_I - g_J)^2 \mu_B^2}{2\hbar^2 \omega_{\text{hf}}} \right) B_z^2 \quad (11)$$

where  $g_I$  is the nuclear spin  $g$ -factor and  $g_J$  is the electron spin  $g$ -factor. We measured the coefficients of linear and quadratic shifts (i.e. the bracketed terms in equation (11)), and found them to be in close agreement with published values of 2785.6 Hz/G and 430.94 Hz/G<sup>2</sup>, respectively [8, 36].

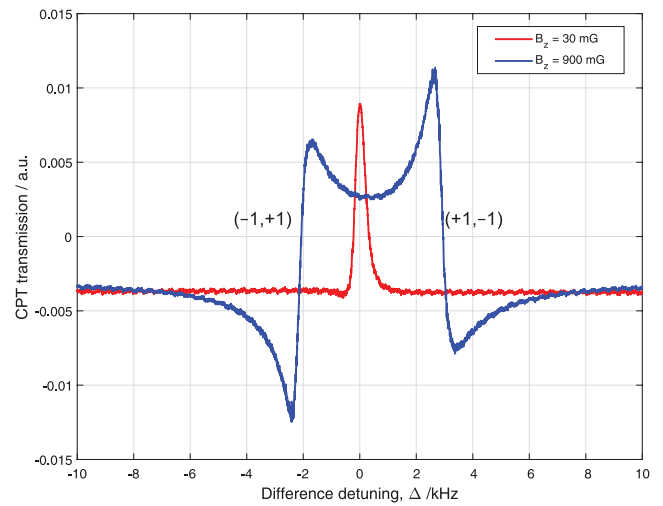


**Figure 11.** Differentially detected MOR CPT resonance generated by  $\text{lin} \parallel \text{lin}$  excitation. The signal is dispersive which is evident at higher magnetic field.

Alternatively, an MOR measurement can be performed in  $\text{lin} \parallel \text{lin}$  excitation scheme for observing MOR CPT resonance with high contrast [28, 29]. In this case, the  $\text{lin} \parallel \text{lin}$  polarized beam is transformed to  $45^\circ \text{lin} \parallel \text{lin}$  using the  $\lambda/2$  plate before the cell and differential detection is performed by subtracting the horizontal (H) and vertical (V) components of the polarized field after the cell using a polarimeter consisting of a polarizing beam splitter, two photodetectors, and a high-speed electronic subtractor. Figure 11 shows the MOR CPT resonance observed at the output of the subtractor. With low magnetic field ( $B_z \simeq 30$  mG), the signal shows a single peak, but with a higher magnetic field ( $B_z \simeq 900$  mG), the dispersive nature of the MOR CPT resonance is evident in the separated resonances corresponding to the  $(-1, +1)$  and  $(+1, -1)$  dark states. Differential detection used in MOR has the advantage of generating background-free CPT resonance with high contrast (close to 100%) and highly suppresses the effects of common-mode fluctuations in laser intensity. However, it suffers from the same limitation as the direct detection  $\text{lin} \parallel \text{lin}$  excitation, exhibiting high magnetic field sensitivity, leading to mid- or long-term clock instability.

Traditionally, circular polarization in the form of  $(\sigma^+, \sigma^+)$  or  $(\sigma^-, \sigma^-)$  has been used in commercial CPT clocks [44–46]. Figure 12 shows the CPT spectrum produced by  $(\sigma^-, \sigma^-)$  excitation resonant with the  $|F' = 2\rangle$  state in  $^{87}\text{Rb}$ . The central CPT resonance at  $\Delta = 0$  is only formed by the  $0-0$  dark state as shown earlier in our simulation result in figure 4. Figure 12 also shows frequency-shifted Zeeman CPT resonances formed by  $(-1, -1)$  and  $(+1, +1)$  dark states with frequency shifts proportional to the applied  $B_z$  ( $\simeq 30$  mG).

The broadening of these Zeeman CPT resonances is attributed to the inhomogeneity of  $B_z$  across the cell length. The strengths of Zeeman CPT resonances are indicative of the atomic populations in the  $(-1, -1)$  and  $(+1, +1)$  dark states. These populations are not equal due to asymmetries in the optical pumping rates into the various Zeeman sublevels, as verified by results of numerical simulations to be described shortly. Although the  $(-1, -1)$  Zeeman states are closer to the

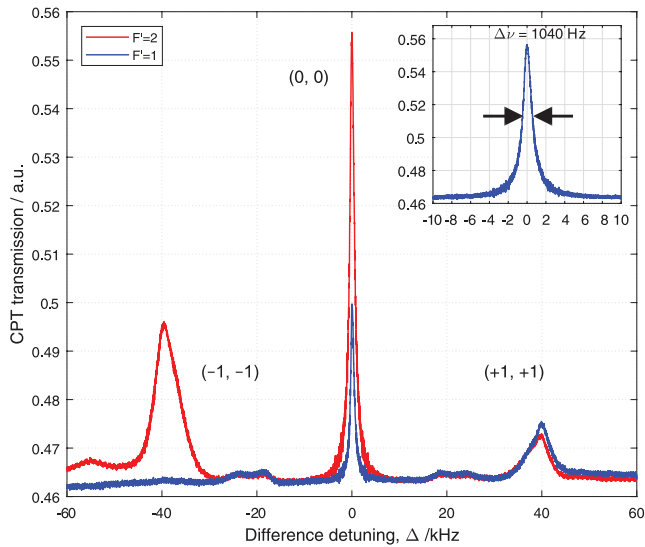


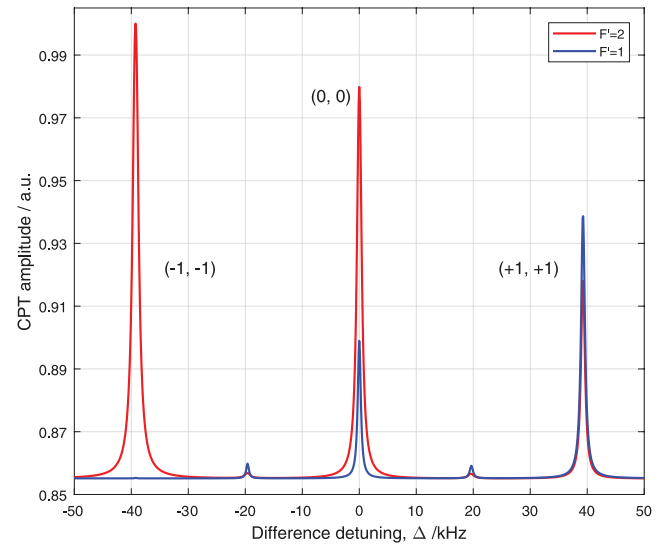
**Figure 12.** CPT spectrum produced by  $(\sigma^-, \sigma^-)$  excitation resonant with the  $|F' = 2\rangle$  state (red) and the  $|F' = 1\rangle$  state (blue) for  $B_z \simeq 30$  mG. The inset in the figure shows the central CPT resonance produced with linewidth = 1.04 kHz and contrast = 16.7%.

$|F = 2, m_F = -2\rangle$  trap state, the  $(-1, -1)$  CPT resonance in figure 12 is found to have a reduced height due to its broadening. Figure 12 also shows weak transverse Zeeman CPT resonances which are formed midway between  $(0, 0)$  and  $(-1, -1)$  or  $(+1, +1)$  resonances due to transverse magnetic fields.

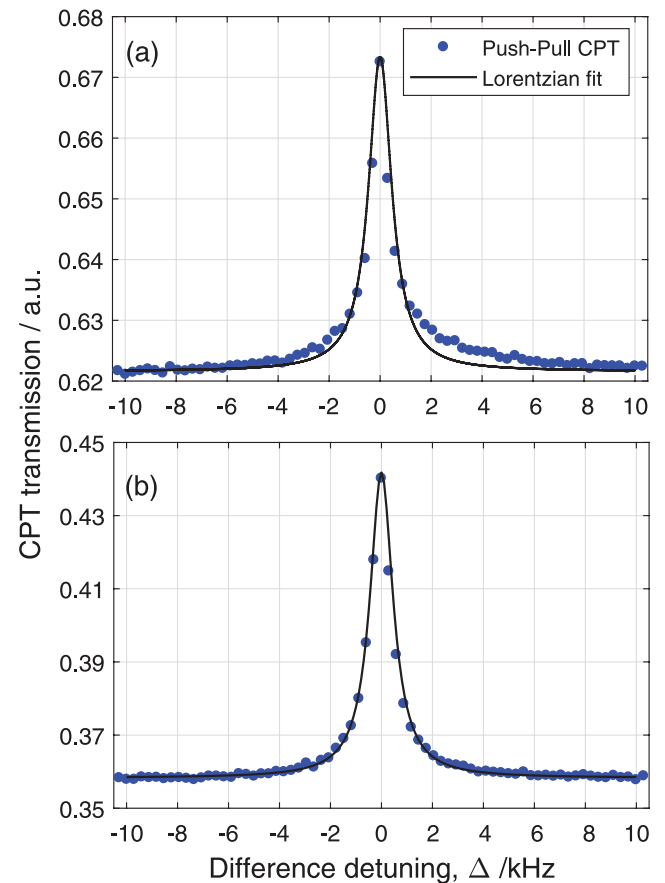
The inset in figure 12 shows the central CPT resonance using a narrow frequency scan (20 kHz) around the two-photon resonance. The linewidth  $\Delta\nu$  and contrast  $C$  of the central CPT resonance are found to be approximately 1.04 kHz and 16.7%, respectively. We observed that  $(\sigma^-, \sigma^-)$  excitation resonant with the  $|F' = 1\rangle$  state produced central CPT resonance with significantly low contrast ( $C \simeq 4.2\%$ ), as shown in figure 12. In addition to the asymmetry in the amplitudes of CPT resonances, it is also seen that Zeeman CPT resonance due to  $(-1, -1)$  dark state cannot be formed in this case.

We used our atomic model (described in section 2) to simulate CPT spectra and compare their contrast for  $(\sigma^-, \sigma^-)$  excitation resonant with the  $|F' = 1\rangle$  or the  $|F' = 2\rangle$  state. These results are shown in figure 13.

For the choice of parameters used in our calculation (i.e.  $\Omega_1 = \Omega_2 = \Gamma/60$ ,  $\Gamma = 6$  MHz,  $\gamma_1 = \gamma_2 = 200$  Hz,  $B_z = 28$  mG and  $B_x \simeq 5$  mG), the central CPT resonance for  $|F' = 2\rangle$  shows a contrast of 13.7% while the one for  $|F' = 1\rangle$  shows reduced contrast 5.3%. This reduction in contrast is due to effective trapping of rubidium atoms in the Zeeman end state  $|F = 2, m_F = 2\rangle$  for resonant excitation with the  $|F' = 1\rangle$  state. Although, the results obtained from our simulation reflect the reduction in contrast, the absolute values of contrast obtained from these results, and the ratios thereof, do not match with our experiment. This is because in the experiment magnetic



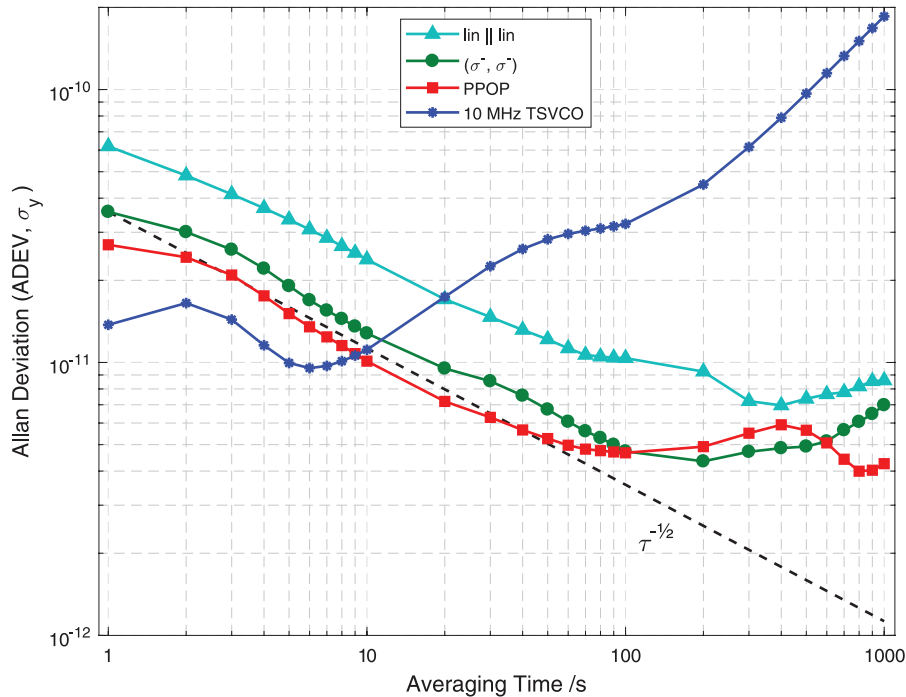
**Figure 13.** CPT spectrum calculated for  $(\sigma^-, \sigma^-)$  excitation resonant with  $|F' = 1\rangle$  (blue) and  $|F' = 2\rangle$  (red) states. The two CPT spectra are made to overlap by using background subtraction. CPT contrast was estimated prior to background subtraction. Following parameters were used in our calculation:  $\Omega_1 = \Omega_2 = \Gamma/60$ ,  $\Gamma = 6$  MHz,  $\gamma_1 = \gamma_2 = 200$  Hz,  $B_z = 28$  mG and  $B_x \simeq 5$  mG.



**Figure 14.** Central CPT resonance produced by lin  $\perp$  lin excitation resonant with (a)  $|F' = 1\rangle$  state (linewidth = 859 Hz, contrast = 7.8%) and (b)  $|F' = 2\rangle$  state (linewidth = 976 Hz, contrast = 19%). The solid lines correspond to Lorentzian fits to the CPT profiles.

**Table 1.** Experimentally measured CPT characteristics for different polarization schemes used in resonant excitation with D1 excited states of  $^{87}\text{Rb}$  atoms (N/A: Not Applicable).

Polarization Scheme	Contrast		Linewidth		Clock Transition	Shot Noise Limited Stability $\sigma_y(\tau = 1 \text{ s})$
	$F' = 1$	$F' = 2$	$F' = 1$	$F' = 2$		
lin    lin	7.5%	N/A	841 Hz	N/A	$(-1, +1), (+1, -1)$	$1.4 \times 10^{-13}$ ( $F' = 1$ )
$(\sigma^-, \sigma^-)$	4.2%	16.7%	780 Hz	1040 Hz	0-0	$7.7 \times 10^{-14}$ ( $F' = 2$ )
lin $\perp$ lin	7.8%	19.0%	859 Hz	976 Hz	0-0	$6.4 \times 10^{-14}$ ( $F' = 2$ )

**Figure 15.** Frequency stability performance of the rubidium CPT clock measured by ADEV with three: lin || lin,  $(\sigma^-, \sigma^-)$  and lin  $\perp$  lin excitations. Dashed line represents  $\sigma_y(\tau) = 3.6 \times 10^{-11} \tau^{-1/2}$ .

field inhomogeneity, beam propagation in the medium, and buffer gas filling can influence CPT contrast, and these effects are not included in our model. The plots in figure 13 show the asymmetries in the amplitudes of the CPT signals for resonant excitation with  $|F' = 2\rangle$  state. The smallest amplitude CPT signal is formed by the  $(+1, +1)$  dark state, which is in qualitative agreement with the results documented in figure 12. The amplitudes of Zeeman CPT signals observed in figure 12 appear to be small compared to those in figure 13 due to broadening by the inhomogeneous magnetic field.

Finally, we investigated the lin  $\perp$  lin excitation scheme by installing the polarization-based interferometer in our experimental setup, as described earlier in section 3. Figure 14 shows the central CPT resonance (with a Lorentzian fit) produced by lin  $\perp$  lin excitation resonant with the  $|F' = 1\rangle$  and  $|F' = 2\rangle$  states, respectively. For comparing the linewidth and contrast of the CPT resonances, the total optical power used in the laser beam is kept the same ( $\approx 70 \mu\text{W}$ ) as that used for the lin || lin and  $(\sigma^-, \sigma^-)$  excitations discussed earlier. The measured values of linewidth and contrast for different excitation schemes are summarized in table 1. The central CPT resonance in the lin  $\perp$  lin excitation resonant with the  $|F' = 2\rangle$  is

mainly formed by the 0-0 dark state, as seen earlier in our simulation result in figure 5(b). We optimized the path difference between the arms of the interferometer to achieve a maximum contrast of 19% for resonant excitation with the  $|F' = 2\rangle$  state. This is nearly 2.4 times higher than that observed for the case where the fields are resonant with the  $|F' = 1\rangle$  excitation. However, the observed linewidth for  $|F' = 1\rangle$  case is found to be slightly smaller than the  $|F' = 2\rangle$  case due to the difference in the strengths of the relevant matrix elements.

As can be seen from the summary in table 1, the lin  $\perp$  lin excitation is clearly superior to the lin || lin excitation, especially in terms of the contrast. It also produces a slightly larger contrast than what can be achieved with the  $(\sigma, \sigma)$  excitations, although the degree of enhancement in contrast is not very significant.

The need to add the interferometer to the cell physics package may give rise to additional complexity (in terms of volume and weight), thus, making lin  $\perp$  lin unsuitable for compact clock designs. However, as mentioned before, a counter-propagating  $\sigma^+$  and  $\sigma^-$  excitation scheme with similar advantages can be adopted in compact clock design employing cold atoms.

We measured the frequency stability of our rubidium CPT clock prototype by employing all three excitation schemes:  $\text{lin} \parallel \text{lin}$ ,  $(\sigma^-, \sigma^-)$  and  $\text{lin} \perp \text{lin}$ . The CPT clock is operated by electronically locking the 10 MHz TSVCO to the peak of the central CPT resonance. The frequency stability (or Allan deviation, ADEV,  $\sigma_y$ ) of the locked oscillator is measured using a phase-noise measurement test probe (Microsemi, 3120A) by referencing it to a rubidium standard (SRS, FS725,  $\sigma_y < 2 \times 10^{-11}$  at integration time,  $\tau = 1$  s). Figure 15 shows a comparison of frequency stabilities for  $\text{lin} \parallel \text{lin}$ ,  $(\sigma^-, \sigma^-)$  and  $\text{lin} \perp \text{lin}$  with the free-running oscillator stability (blue line). The free-running oscillator exhibits a short-term stability,  $\sigma_y \simeq 1.4 \times 10^{-11}$  at  $\tau = 1$  s and relatively high instability at longer integration time: for example,  $\sigma_y \simeq 1.9 \times 10^{-10}$  at  $\tau = 1000$  s. The CPT locked oscillator shows improved long-term stabilities for all excitations: for example,  $\sigma_y \simeq 4.7 \times 10^{-12}$  at  $\tau = 100$  s using  $(\sigma^-, \sigma^-)$  excitation. It should be noted that a well-engineered CPT clock should produce close to shot-noise limited stability which is given by

$$\sigma_y(\tau) = \frac{1}{Q} \frac{1}{\text{SNR}} \tau^{-1/2}, \quad (12)$$

where  $Q = \nu_{\text{hf}}/\Delta\nu$  represents the quality factor of CPT resonance, and SNR is the signal-to-noise ratio for integration over 1 s. The estimated shot noise limited stability values are given in table 1. The dashed line drawn in figure 15 shows the expected shot-noise limited stability (i.e.  $\sigma_y \propto \tau^{-1/2}$ ) for the  $(\sigma^-, \sigma^-)$  excitation with a starting stability  $\sigma_y \simeq 3.6 \times 10^{-11}$  at  $\tau = 1$  s.

The CPT clocks for all three excitations do not seem to produce shot-noise limited stability for  $\tau$  exceeding 100 s. Frequency stability better than  $10^{-12}$  has been achieved in rubidium CPT clocks at  $\tau$  exceeding 1000 s [1, 47]. The performance of our CPT clock is currently limited by various sources of long-term frequency drifts in the system. The major source of frequency drift is related to optical power drift associated with the fiber pigtailed EOM. The power drift is caused by stress and temperature-induced polarization rotation in the fiber, coupled with polarization-dependent modulation properties of the EOM. Other sources of frequency drifts such as cell temperature instability and magnetic field fluctuation are also affecting the long-term stability performance of our CPT clock. Under these circumstances, a comparison of frequency stabilities shown in figure 15 indicate that  $\text{lin} \parallel \text{lin}$  excitation exhibits the poorest performance of all, both in terms of short-term (due to poor signal contrast) and long-term (possibly due to its high magnetic field sensitivity) stabilities. A long-term stability of  $\sigma_y \simeq 9 \times 10^{-12}$  for  $\tau \simeq 150$  s is found in this case. The highest short-term stability ( $\sigma_y \simeq 2.7 \times 10^{-11}$ ) is found in the case of  $\text{lin} \perp \text{lin}$  excitation due to its high CPT contrast. However, the long-term performance of the  $\text{lin} \perp \text{lin}$  CPT clock is affected due to imperfections in the interferometer. Fluctuations in polarization states of the sidebands are caused by vibrations and thermal expansions in the interferometer. Small extinction ratio of the PBS leads to polarization leakage in the arms and hence, power drift at the output of the interferometer. These

problems can be mitigated by employing a high extinction PBS in a monolithically designed interferometer.

## 5. Conclusion

We have investigated the comparative properties of  $\text{lin} \parallel \text{lin}$ ,  $(\sigma, \sigma)$ , and  $\text{lin} \perp \text{lin}$  excitation schemes for producing narrow linewidth, high contrast, magnetically-insensitive CPT resonances in the D1 manifold of  $^{87}\text{Rb}$  atoms. The performances of these schemes are studied, experimentally as well as theoretically, keeping in mind their application in compact and high-performance CPT clock development using a vapor cell. The results show higher magnetic field sensitivity of the CPT resonance produced by  $\text{lin} \parallel \text{lin}$  excitation. For  $(\sigma, \sigma)$  excitation, we found that the CPT contrast is dependent on the transition used for locking the laser frequency, and reached a maximum value 16.7% for lasers resonant with the  $|F' = 2\rangle$  state. The theoretical calculations characterize the magnetic field dependence of the central CPT resonance formed by different excitations, and also show that additional Zeeman CPTs could be formed in the presence of a transverse component of a bias magnetic field, arising from imperfect alignments of the optical fields. The experimental studies were carried out in a clock prototype consisting of a laboratory scale Rb vapor cell physics package. CPT contrast close to 20% was measured using the  $\text{lin} \perp \text{lin}$  excitation. Frequency stability performances of the rubidium clock prototype were measured by employing  $\text{lin} \parallel \text{lin}$ ,  $(\sigma^-, \sigma^-)$  and  $\text{lin} \perp \text{lin}$  excitation schemes. We attained a short-term stability  $\sigma_y \simeq 2.7 \times 10^{-11}$  for  $\tau = 1$  s and a long-term stability  $\sigma_y \simeq 4.3 \times 10^{-12}$  for  $\tau = 1000$  s for the  $\text{lin} \perp \text{lin}$  excitation.

## Acknowledgments

The authors acknowledge the support received from the DoD HBCU/MI (#62818-PH-REP), NASA-MIRO (#NNX15AP84A), NSF-CREST (#1242067), and ARO DURIP (#66892-EV-RIP) grants for conducting this research.

## References

- [1] Merimaa M, Lindvall T, Tittonen I and Ikonen E 2003 All-optical atomic clock based on coherent population trapping in  $^{85}\text{Rb}$  *JOSA B* **20** 273–9
- [2] Knappe S, Schwindt P, Shah V, Hollberg L, Kitching J, Liew L and Moreland J 2005 A chip-scale atomic clock based on  $^{87}\text{Rb}$  with improved frequency stability *Opt. Express* **13** 1249–53
- [3] Knappe S 2007 MEMS atomic clocks *Comprehensive Microsystems* vol 3, ed Y Gianchandani et al (New York: Elsevier) pp 571–612
- [4] Bloch M, Pascaru I, Stone C and McClelland T 1993 Subminiature rubidium frequency standard for commercial applications *IEEE Int. Frequency Control Symp.* pp 164–77
- [5] Ho J, Pascaru I, Stone C and McClelland T 1998 New rubidium frequency standard designs for telecommunications applications *IEEE Int. Frequency Control Symp.* pp 80–3

- [6] Prestage J D and Weaver G L 2007 Atomic clocks and oscillators for deep-space navigation and radio science *Proc. IEEE* **95** 2235–47
- [7] Koyama Y, Matsuura H, Atsumi K, Nakamuta K and Maruyama I 2000 An ultra-miniature rubidium frequency standard *IEEE/EIA Int. Frequency Control Symp. and Exhibition* pp 694–9
- [8] Esnault F-X, Blanshan E, Ivanov E N, Scholten R E, Kitching J and Donley E A 2013 Cold-atom double- $\Lambda$  coherent population trapping clock *Phys. Rev. A* **88** 42120
- [9] Zibrov S A, Novikova I, Phillips D F, Walsworth R L, Zibrov A S, Velichansky V L, Taichenachev A V and Yudin V I 2010 Coherent-population-trapping resonances with linearly polarized light for all-optical miniature atomic clocks *Phys. Rev. A* **81** 1–7
- [10] Boudot R, Dziuban P, Hasegawa M, Chutani R K, Galliou S, Giordano V and Gorecki C 2011 Coherent population trapping resonances in Cs–Ne vapor microcells for miniature clocks applications *J. Appl. Phys.* **109** 14912
- [11] Goka S 2010  $^{85}\text{Rb}$  D1-line coherent-population-trapping atomic clock for low-power operation *Japan. J. Appl. Phys.* **49** 0628011–4
- [12] Zhang Y, Yang W, Shuangyou Z and Zhao J 2016 Rubidium chip-scale atomic clock with improved long-term stability through light intensity optimization and compensation for laser frequency detuning *J. Opt. Soc. Am. B* **33** 1756–63
- [13] Shah V and Kitching J 2010 *Advances in Coherent Population Trapping for Atomic Clocks* vol 59 (New York: Elsevier) ([https://doi.org/10.1016/S1049-250X\(10\)59002-5](https://doi.org/10.1016/S1049-250X(10)59002-5))
- [14] Vanier J 2005 Atomic clocks based on coherent population trapping: a review *Appl. Phys. B* **81** 421–42
- [15] Farkas D M, Zozulya A and Anderson D Z 2010 A compact microchip atomic clock based on all-optical interrogation of ultra-cold trapped Rb atoms *Appl. Phys. B* **101** 705–21
- [16] Donley E A, Blanshan E, Esnault F-X and Kitching J 2014 Frequency biases in a cold-atom coherent population trapping clock *IEEE Int. Frequency Control Symp.* (<https://doi.org/10.1109/FCS.2014.6859921>)
- [17] Zibrov S, Velichansky V L, Zibrov A S, Taichenachev A V and Yudin V I 2005 Experimental investigation of the dark pseudoresonance on the D1 line of the  $^{87}\text{Rb}$  atom excited by a linearly polarized field *J. Exp. Theor. Phys. Lett.* **82** 477–81
- [18] Kazakov G, Matisov B, Mazets I, Mileti G and Delporte J 2005 Pseudoresonance mechanism of all-optical frequency-standard operation *Phys. Rev. A* **72** 1–6
- [19] Taichenachev A V, Yudin V I, Velichansky V L and Zibrov S A 2005 On the unique possibility to increase significantly the contrast of dark resonances on D1 line of  $^{87}\text{Rb}$  *J. Exp. Theor. Phys. Lett.* **82** 398–403
- [20] Mikhailov E E, Horrom T, Belcher N and Novikova I 2010 Performance of a prototype atomic clock based on linlin coherent population trapping resonances in Rb atomic vapor *J. Opt. Soc. Am. B* **27** 417–22
- [21] Zanon T, Guerandel S, De Clercq E, Holleville D, Dimarcq N and Clairon A 2005 High contrast ramsey fringes with coherent-population-trapping pulses in a double lambda atomic system *Phys. Rev. Lett.* **94** 193002
- [22] Kargapoltsev S V, Kitching J, Hollberg L, Taichenachev A V, Velichansky V L and Yudin V I 2004 High-contrast dark resonance in  $\sigma^+ - \sigma^-$  optical field *Laser Phys. Lett.* **1** 495–99
- [23] Jau Y Y, Miron E, Post A B, Kuzma N N and Happer W 2004 Push–pull optical pumping of pure superposition states *Phys. Rev. Lett.* **93** 160802
- [24] Liu X, Mérola J M, Guérandel S, Gorecki C, De Clercq E and Boudot R 2013 Coherent-population-trapping resonances in buffer-gas-filled Cs-vapor cells with push–pull optical pumping *Phys. Rev. A* **87** 013416
- [25] Abdel Hafiz M and Boudot R 2015 A coherent population trapping Cs vapor cell atomic clock based on push–pull optical pumping *J. Appl. Phys.* **118** 124903
- [26] Breschi E, Grujic Z D, Knowles P and Weis A 2014 A high-sensitivity push–pull magnetometer *Appl. Phys. Lett.* **104** 1–5
- [27] Shah V, Knappe S, Hollberg L and Kitching J 2007 High-contrast coherent population trapping resonances using four-wave mixing in  $^{87}\text{Rb}$  *Opt. Lett.* **32** 1244–6
- [28] Tan B, Tian Y, Lin H, Chen J and Gu S 2015 Noise suppression in coherent population-trapping atomic clock by differential magneto-optic rotation detection *Opt. Lett.* **40** 3703–6
- [29] Rosenbluh M, Shah V, Knappe S and Kitching J 2006 Differentially detected coherent population trapping resonances excited by orthogonally polarized laser fields *Opt. Express* **14** 6588–94
- [30] Momeen M U, Rangarajan G and Deshmukh P C 2007 Magneto optical rotation in the Doppler-broadened spectrum of Rb atoms in intermediate fields *J. Phys. Conf. Ser.* **80** 1–7
- [31] Liang S-Q, Yang G-Q, Xu Y-F, Lin Q, Liu Z-H and Chen Z-X 2014 Simultaneously improving the sensitivity and absolute accuracy of CPT magnetometer *Opt. Express* **22** 6837
- [32] Budker D, Kimball D, Rochester S, Yashchuk V and Zolotarev M 2000 Sensitive magnetometry based on nonlinear magneto-optical rotation *Phys. Rev. A* **62** 043403
- [33] Yang A-L, Yang G-Q, Xu Y-F and Lin Q 2014 High contrast atomic magnetometer based on coherent population trapping *Chin. Phys. B* **23** 027601
- [34] Pati G S, Warren Z, Yu N and Shahriar M S 2015 Computational studies of light shift in a Raman–Ramsey interference-based atomic clock *J. Opt. Soc. Am. B* **32** 388–94
- [35] Shahriar M S, Wang Y, Krishnamurthy S, Tu Y, Pati G S and Tseng S 2014 Evolution of an N-level system via automated vectorization of the Liouville equations and application to optically controlled polarization rotation *J. Mod. Opt.* **61** 351–67
- [36] Steck D A 2015 *Rubidium 87 D Line Data* (<http://steck.us/alkalidata>) (revision 2.1.5, 13 January 2015)
- [37] Zanon-Willette T, De Clercq E and Arimondo E 2011 Ultrahigh-resolution spectroscopy with atomic or molecular dark resonances: exact steady-state line shapes and asymptotic profiles in the adiabatic pulsed regime *Phys. Rev. A* **84** 1–17
- [38] Shahriar M S, Hemmer P R, Katz D P, Lee A and Prentiss M G 1997 Dark-state-based three-element vector model for the stimulated Raman interaction *Phys. Rev. A* **55** 2272–82
- [39] Margalit L, Rosenbluh M and Wilson-Gordon A D 2013 Coherent-population-trapping transients induced by a modulated transverse magnetic field *Phys. Rev. A* **88** 023827
- [40] Cox K, Yudin V I, Taichenachev A V, Novikova I and Mikhailov E E 2011 Measurements of the magnetic field vector using multiple electromagnetically induced transparency resonances in Rb vapor *Phys. Rev. A* **83** 2–5
- [41] Goka S 2009  $^{85}\text{Rb}$  coherent-population-trapping atomic clock with low power consumption *Japan. J. Appl. Phys.* **48** 82202
- [42] Snoddy J, Li Y, Ravet F and Bao X 2007 Stabilization of electro-optic modulator bias voltage drift using a lock-in amplifier and a proportional-integral-derivative controller in a distributed Brillouin sensor system *Appl. Opt.* **46** 1482
- [43] Taichenachev A V, Yudin V I, Velichansky V L, Kargapoltsev S V, Wynands R, Kitching J and Hollberg L 2004 High-contrast dark resonances on the D1 line of alkali metals in the field of counterpropagating waves *J. Exp. Theor. Phys. Lett.* **80** 236–40

- [44] Deng J, Vlitaz P, Taylor D, Perletz L and Lutwak R 2008 A commercial CPT rubidium clock *Proc. European Frequency and Time Forum (EFTF) (Toulouse, FR, 22–25 April 2008)* E3B01-0099
- [45] Lutwak R, Emmons D, Riley W and Garvey R 2002 The chip-scale atomic clock - coherent population trapping vs. conventional interrogation *34th Annual Precise Time and Time Interval (PTTI) Meeting* pp 539–50
- [46] Lutwak R 2009 The chip-scale atomic clock—recent developments 2009 *IEEE Int. Frequency Control Symp. Joint with the 22nd European Frequency and Time Forum* pp 573–7
- [47] Zhu M 2003 High contrast signal in a coherent population trapping based atomic frequency standard application *Proc. IEEE Int. Frequency Control Symp. (IEEE)* pp 16–21